ARTICLE

Atomic-Scale Picture of the Composition, Decay, and Oxidation of Two-Dimensional Radioactive Films

Alex Pronschinske,[†] Philipp Pedevilla,[‡] Benjamin Coughlin,[†] Colin J. Murphy,[†] Felicia R. Lucci,[†] Matthew A. Payne,[§] Andrew J. Gellman,[§] Angelos Michaelides,*[,‡] and E. Charles H. Sykes*[,†]

[†]Department of Chemistry, Tufts University, 62 Talbot Avenue, Medford, Massachusetts 02155, United States
[‡]Thomas Young Centre, London Centre for Nanotechnology and Department of Chemistry, University College London, London WC1E 6BT, United Kingdom
[§]Department of Chemical Engineering, Carnegie Mellon University, Pittsburgh, Pennsylvania 15213, United States

Ⓢ *Supporting Information*

ABSTRACT: Two-dimensional radioactive ^{125}I monolayers are a recent development that combines the fields of radiochemistry and nanoscience. These Au-supported monolayers show great promise for understanding the local interaction of radiation with 2D molecular layers, offer different directions for surface patterning, and enhance the emission of chemically and biologically relevant low-energy electrons. However, the elemental composition of these monolayers is in constant flux due to the nuclear transmutation of ^{125}I to ^{125}Te, and their precise composition and stability under ambient conditions has yet to be elucidated. Unlike I, which is stable and unreactive when bound to Au, the newly formed Te atoms would be expected to be more reactive. We have used electron emission and X-ray photoelectron spectroscopy (XPS) to quantify the emitted electron energies and to track the film composition in vacuum and the effect of exposure to ambient conditions. Our results reveal that the Auger electrons emitted during the ultrafast radioactive decay process have a kinetic energy corresponding to neutral Te. By combining XPS and scanning tunneling microscopy experiments with density functional theory, we are able to identify the reaction of newly formed Te to TeO_2 and its subsequent dimerization. The fact that the Te_2O_4 units stay intact during major lateral rearrangement of the monolayer illustrates their stability. These results provide an atomic-scale picture of the composition and mobility of surface species in a radioactive monolayer as well as an understanding of the stability of the films under ambient conditions, which is a critical aspect in their future applications.

KEYWORDS: *radioactive, 2D material, self-sustaining electron source, iodine-125, electron emission, STM*
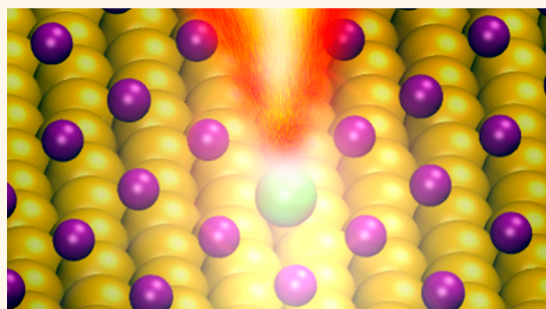
The interaction of high-energy radiation (γ-rays, X-rays, α- and β-particles) with matter produces not only primary impact damage but also large numbers of nonthermal secondary electrons (<10 eV) along the radiation track.[1−3] Although these electrons are below the ionization energies of biologically relevant molecules, they initiate radiation-induced chemical reactions, making them arguably the most important species in radiation chemistry.[2,4,5] The bond-breaking mechanism at energies less than 10 eV is primarily from dissociative electron attachment, during which a short-lived negative ion of the molecule is formed and then dissociates into a radical fragment and an anionic fragment.[6,7] At higher energies, electron impact excitation (>6 eV) and ionization (>10 eV) events begin to occur. Even if the electron does not react directly with a DNA molecule, for example, indirect effects such as the formation of solvated electrons can

lead to genome damage.[8−11] As a result of their high reactivity and short path length, any source of low-energy electrons must be within ∼10 nm of a target to induce reaction chemistry.[12] As a method to escape the need for an external radiation source to power the production of low-energy electrons, Pronschinske *et al.* reported on single-atom-thick, ordered radioactive films of ^{125}I on gold that can be constructed on the same nanometer scale as a low-energy electron's range. These films provide a self-sustaining source of copious amounts of low-energy electrons in the 0−10 eV range.[1] Electrons in this low-energy range have been shown to cause both DNA single- and double-

strand breaks in electron-stimulated desorption experiments and are also implicated in the increased antitumor efficacy of gold nanoparticles irradiated with X-rays.[13−16] As a first step toward application of this new approach for local low-energy electron delivery, for example, conjugated to gold nano-particles,[17−23] characteristics such as the radioactive film stability and reactivity in an ambient environment must be understood.

In terms of applications as a self-sustaining nanoemitter, given the massive amount of energy released during the nuclear decay of radioactive ^{125}I (185 keV), one must consider the stability of the material before, during, and after nuclear decay as well as the effect of ambient conditions. The ^{125}I/Au combination is well-suited for application because of the strong I−Au bond[24,25] and negligible neutrino-induced nuclear recoil of ^{125}I (0.1 eV). This recoil energy is very low compared to that of other isotopes that decay by electron capture (EC) or through emission of an α- or β-particle.[26−30] The decay of ^{125}I via EC results in a nuclear proton and a core-level electron being converted to a neutron with the release of an electron neutrino and, hence, elemental transmutation of ^{125}I into ^{125}Te. While there have been some studies of Te films on Au(111), they have mostly focused on depositing the element with electrochemical control.[31,32] Another potential chemical instability resulting from nuclear decay is Coulomb explosion that results from slow neutralization of the radionuclide following ultrafast emission of copious amounts of its valence electrons,[33−36] which for ^{125}I can be upward of 20 electrons as predicted by Monte Carlo studies.[37] When such highly charged radionuclides have insufficient electronic coupling to their environment, for example, ^{55}Fe-containing alkanethiol SAMs, their rate of neutralization falls below the time scale of atomic motion. This leads to neighboring atoms becoming positively charged and causing local damage through electrostatic repulsion and ejection of ions and charged molecular fragments.[33]

In this study, we use X-ray photoelectron spectroscopy (XPS) to probe the surface composition of radioactive ^{125}I/Au films over time and after exposure to air. This technique allows us to quantify the elemental species and their oxidation states with high surface sensitivity.[38] Density functional theory (DFT) calculations were employed to quantify the binding strength of both the radionuclide ^{125}I and daughter ^{125}Te to the Au substrate. Furthermore, we used DFT calculations to examine the reactivity of the newly formed Te atoms with a range of common molecules present under ambient conditions. This work revealed that the most exothermic reactions involved oxidation of Te to TeO_2. This oxidized Te (in a Te^{4+} oxidation state) was observed by XPS after film exposure to ambient conditions, and scanning tunneling microscopy (STM) revealed the presence of isolated dimers in the film which DFT predicted are thermodynamically preferred Te_2O_4 species formed by two interacting TeO_2 units. Overall, these results look promising in terms of future applications of ^{125}I/Au devices as both the radionuclide and daughter product remain strongly bound to the Au surface during both nuclear decay and exposure to ambient conditions.

RESULTS AND DISCUSSION

^{125}I/Au(111) samples were made using the established ambient drop-casting method at PerkinElmer (Billerica, MA); a photograph of the drop-casting procedure is shown in Figure 1A.[1] The samples were then transferred to Tufts and Carnegie
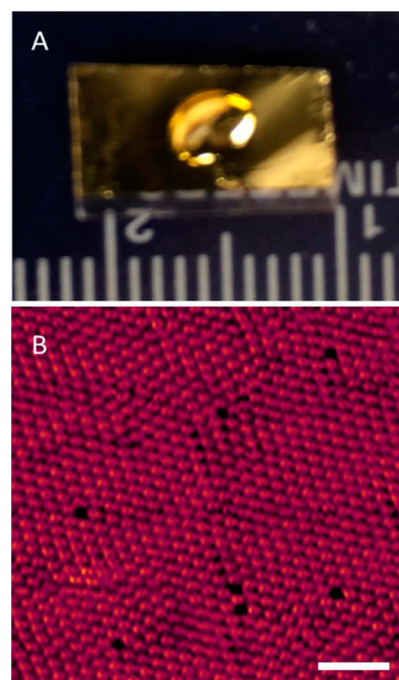
Figure 1. (A) Photograph of the deposition of an aqueous solution of Na^{125}I (161 μM) on Au(111) using an ambient drop-casting method. (B) Resulting ^{125}I monolayer as imaged using scanning tunneling microscopy ($V = -0.4$ V, $I = 0.1$ nA, scale bar = 2 nm).

Mellon Universities under ambient conditions over a period of 1−2 days. Figure 1B shows a high-resolution STM image of a sample in which the I atoms of the monolayer film are clearly resolved.

Single-atom depressions are randomly distributed in the monolayer structure that correspond to Te atoms formed from the nuclear transmutation of ^{125}I.[1] Given the copious amounts of electrons that are emitted by these samples, we will first discuss our electron emission studies that report on the charge state of the decaying atoms before moving on to measurements of the composition and oxidation by XPS, and DFT modeling of various reaction pathways.

The radioactive decay of ^{125}I (half-life = 60 days) is a multistep process consisting of (in order) EC, an electron emission cascade, relaxation of the excited ^{125}Te nucleus, and a second electron emission cascade. These cascades are driven by Auger relaxations, two-electron processes in which an ejected electron leaves behind a hole which is filled by a higher-lying electron, and the additional energy is released in the form of a second electron. This second electron is called the Auger electron and has a kinetic energy dependent only on the charge state of the atom and not the initial excitation energy. The MNN Auger transition of the element Te is lower in energy than most of the emitted electrons and typically occurs near the end of the electron emission cascade. By placing the ^{125}I/Au samples in ultrahigh vacuum (UHV), we are able to use a concentric hemispherical electron energy analyzer to measure the energy of these Auger electrons and gain a window into the charge state of the newly formed Te atom during the ultrafast electron emission cascades. Electron emission from radioactive decay of ^{125}I occurs in two stages.[46] Briefly, in the first step called EC, a core electron tunnels into the nucleus and combines with a proton. This leaves a core hole which releases its energy on a 0.1−10 fs time scale via X-rays and Auger

electrons. The Te nucleus is left in an excited state with a half-life of ~2 ns which, 7% of the time, decays *via* γ-ray emission. In the other 93% of cases, the excess nuclear energy is released *via* ejection of an inner shell electron, leaving another core hole which decays *via* a cascade of events similar to the first step. Therefore, as mentioned in the introduction, charging of the newly formed Te atom depends on the relative rates of electron emission and neutralization from surrounding Au atoms. Given that Auger emission is dependent only on the charge state of the atom and not the source of the initial excitation, the kinetic energy of these transitions provide direct insight into how fast the newly formed Te atom can neutralize during these ultrafast cascades.

In Figure 2, we observe the Te MNN Auger electron emission peaks at kinetic energies of 483 and 493 eV, which is
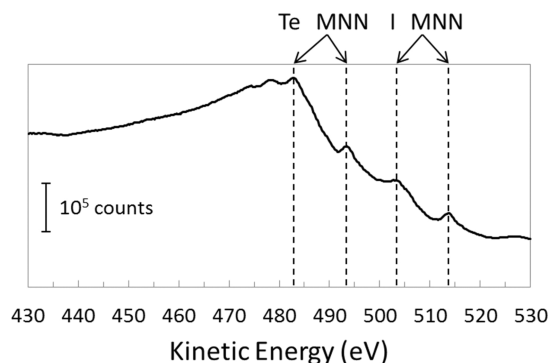

Figure 2. Kinetic energy spectrum of electron emission during radioactive decay of ^{125}I on Au(111). Te MNN and I MNN Auger electron emission peaks are marked.

at the same energy as a neutral Te atom.[47] Based on literature photoemission data, one can expect that the Te MNN Auger peak will shift by around −1 eV (in kinetic energy) for each additional +1 charge on the Te atom.[47] Monte Carlo studies of the decay of ^{125}I atoms have shown that, on average, ~13 electrons are ejected per decay event.[33] Therefore, if the ^{125}Te were charging up to +13 after being formed from ^{125}I, the Te MNN Auger peak would appear drastically shifted to around 470 eV. However, it is clear from the data in Figure 2 that, despite the ultrafast electron emission cascades following a ^{125}I EC event, the daughter Te atom does not charge up. In addition to the two predominant Te^0 MNN Auger electron emission peaks, we observe a smaller pair of peaks at 503 and 514 eV corresponding to I MNN Auger electron emission peaks. This would indicate that some of the surrounding ^{125}I atoms that have not yet decayed are excited by radiation in the form of either photons or electrons emitted during the radioactive decay.

In order to further our understanding of the lack of charging, that is, fast neutralization of the Te atom undergoing the electron emission cascades by Au, we used DFT to examine the nature of the Te/Au interaction in the I/Te/Au(111) overlayer. To this end, we examined how the valence electron density rearranges upon formation of the Te/Au bond. This is shown in Figure 3, where we plot how the electron density rearranges upon subtracting from the total density of the complete I/Te/Au(111) overlayer the density of the I/Au(111) overlayer and an isolated Te atom. This plot therefore captures how the valence electron density rearranges upon formation of the Te—Au adsorption bond in the presence of the I/Au(111)
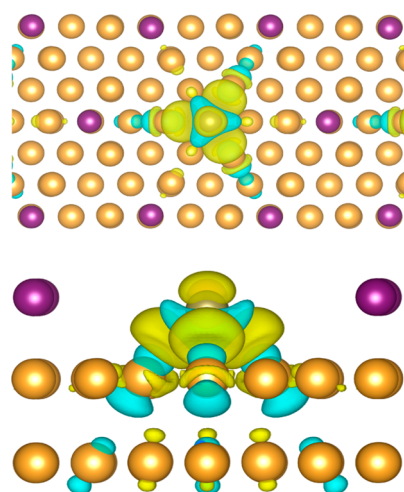

Figure 3. Electronic density rearrangement upon Te adsorption on Au(111). Specifically, $\Delta\rho = \rho_{total} - \rho_{I/Au} - \rho_{Te}$ is plotted, where ρ_{total} is the charge density of the complete I/Te/Au(111) structure, $\rho_{I/Au}$ the charge density of the I/Au(111) overlayer, and ρ_{Te} the charge density of an isolated Te atom. The Te atom is located in a hollow site and interacts strongly with its three closest Au neighbors. Regions of charge increase are shown in blue, and areas with charge depletion are shown in yellow, both at an isovalue of 0.002 e/Å^3. The charge density difference from a top view and side view are shown in the top and bottom panels, respectively. For clarity, only the top few layers of the gold slab are shown. Gold atoms are colored in gold and iodine atoms in purple. The Te atom is located at the center of the charge density difference plot.
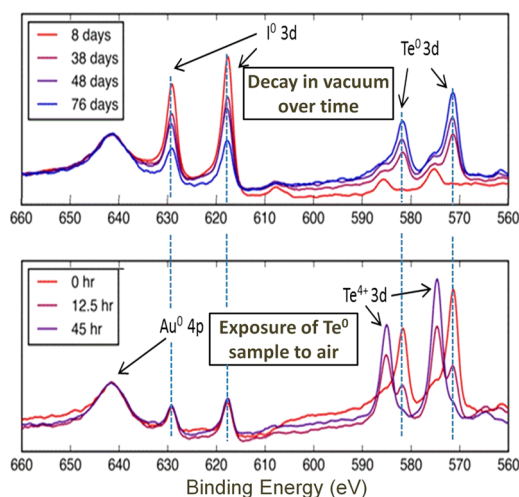
Figure 4. XPS spectra showing nuclear transmutation of I to Te and the effect of exposure to air. The top plot shows the I 3d core-level signals decreasing and the Te^{0+} core levels increasing over time as the ^{125}I decays into ^{125}Te by electron capture. The bottom plot shows the formation of Te^{4+} caused by exposing a surface of Te^0 formed in vacuum to ambient conditions for a number of hours.

overlayer. From Figure 3, we can identify quite significant charge rearrangement around the Te and three Au atoms to which it is directly bonded. There is also smaller but not insignificant rearrangement of electron density in some of the second-layer Au atoms. The charge rearrangement implies that mixed Te(p)—Au(d) states have formed, and that there is a degree of coupling between Te and the Au substrate. Indeed, we have directly confirmed the formation of mixed Te(p)—Au(d) states by analyzing the individual Kohn−Sham states in
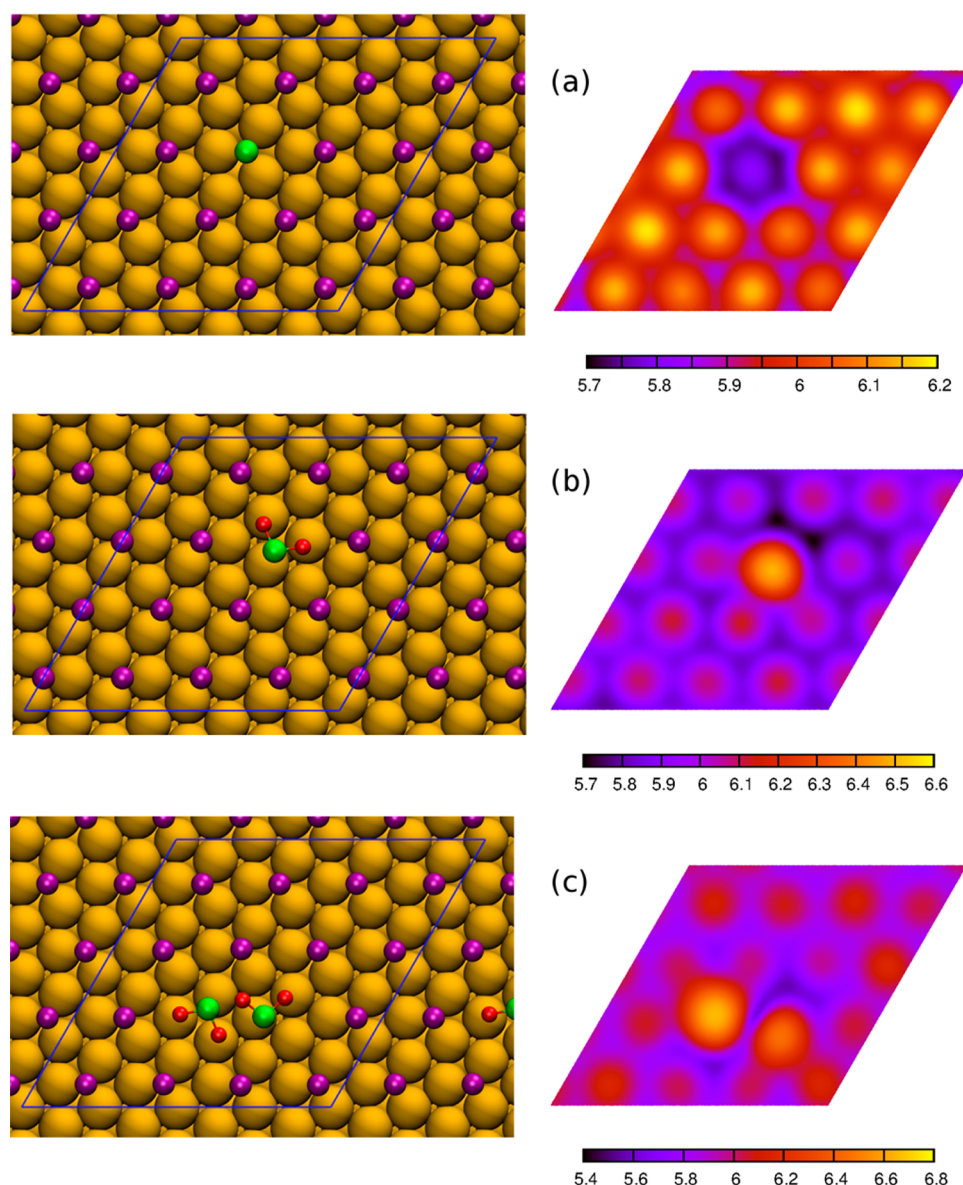
Figure 5. (a) DFT-optimized structure of a Te atom (green) in an I (violet) overlayer with its corresponding simulated STM image. The Te atom appears as a depression relative to the surrounding I atoms. (b) Single TeO_2 species in an I overlayer, which appears as a protrusion compared to the I atoms. (c) Thermodynamically preferred Te_2O_4 and corresponding simulated STM. The dimer appears as two bright spots relative to the I atoms. Simulated STM images are shown for a constant LDOS of 1×10^{-9} $e/Å^3$.

the system. We show these data in the Supporting Information Figure SI2. This orbital mixing and fairly long-range charge rearrangement means that during the nuclear-decay-induced electron emission cascade the positive charge created at the Te atom will be spread out over many Au atoms and be neutralized by the electron sea of the extended Au surface to such an extent that the effective charge on the Te atom is zero, as measured experimentally.

By working in UHV, we are able to study the as-formed oxidation state of the ^{125}Te atom before and then after exposure to ambient conditions. After a few weeks of ^{125}I radioactive decay in UHV, repeated XPS measurements reveal that that the daughter Te 3d core-level doublet that grows over time is at 573 eV, corresponding to neutral Te^0, as shown in Figure 4.[48,49] All charge density decomposition schemes involve a certain level of arbitrariness; however, performing a Bader population analysis of our DFT adsorption system yields a partial charge

on the Te bound to Au of +0.22e, which is in good agreement with our XPS measurement and is consistent with the similar electronegativities of Au and Te. Importantly, from our DFT calculations, we see that the newly formed ^{125}Te is even more tightly bound to a bare Au(111) surface (3.41 eV) than ^{125}I (2.21 eV), which explains the film's stability during radioactive decay as the nuclear recoil energy is ~0.1 eV. If the recoil energy was greater than the Te–Au bond strength, the daughter Te atom could leave the surface.

The ^{125}Te atoms in the film (Te being one group to the left of I in the periodic table) are under-coordinated and, like the surface of bulk Te, are more susceptible to chemical reactions. Upon arrival from PerkinElmer, the ^{125}I samples always display a small Te 3d doublet at 576 and 586 eV,[48,49] which corresponds to Te^{4+}, as shown in Figure 4, which is formed in transit. Through incremental exposure to ambient conditions and measurement by XPS, we see that the newly formed Te^0

undergoes oxidation to the Te^{4+} oxidation state. This reaction is kinetically limited as it takes about 45 h to fully oxidize the surface Te. To understand the details of this oxidation process, we considered a range of reactions between (newly formed) Te and common species present under ambient conditions such as O_2, CO, H_2O, and H_2 with DFT (see Supporting Information for full details). Formation energies of all the species, which could potentially form from reaction with atmospheric compounds, are summarized in Table SI1. The most stable reaction product for each reaction is shown in Figure SI1. Our DFT calculations indicate that the formation of TeO_2 starting from a Te atom adsorbed on Au and an oxygen molecule is exothermic by −1.24 eV. None of the other reactions studied with DFT were as thermodynamically favorable as oxidation by molecular O_2. Based on the XPS and DFT results, we therefore assign the oxidized species to be TeO_2.

Further support of the ambient oxidation product of Te being TeO_2 comes from DFT-simulated STM images. In Figure 5, we compare the DFT-simulated STM images of a Te atom, a single TeO_2 species, and a Te_2O_4 dimer in a I monolayer on Au(111). Only the simulated image for TeO_2 dimers matches the STM experiment (shown in Figure 6); we therefore assign
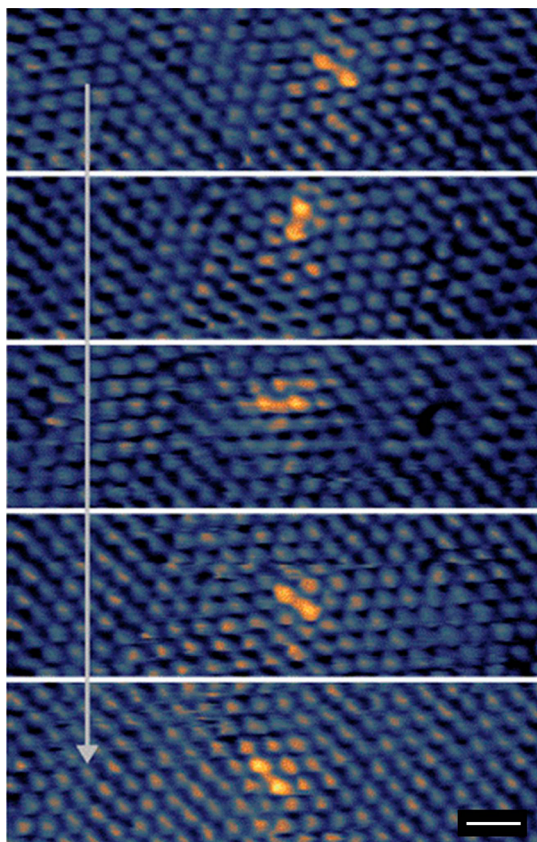
Figure 6. Diffusion of the TeO_2 dimer within the I monolayer. Shown is a series of consecutive STM images taken over a set location (V = 0.1 V, I = 0.1 nA, scale bar = 1 nm).

each of the protrusions seen in the STM images as TeO_2 species. The DFT-computed energy difference between noninteracting TeO_2 units on Au(111) and TeO_2 dimers on Au(111) is −0.1 eV, which explains why nearly all of the TeO_2 imaged with STM in the form of dimers. Figure 5c shows that the two TeO_2 molecules are held together by a weak intermolecular Te−O bond. At 2.45 Å, this Te−O bond is significantly longer that the intramolecular bond, which is just 1.90 Å.

During time-lapse STM imaging of the ^{125}I/Au(111) samples, we observed tip-induced diffusion of the I overlayer, as seen in Figure 6. The experiments were performed at 5 K; therefore, we can rule out any effect of thermal motion. The TeO_2 dimers served as "markers" in the I film that allowed us to assess the degree of mobility, which is not possible in pure I overlayers on Au as there are no reference points in the overlayer. Figure 6 shows a sequence of these time-lapse images in which a TeO_2 dimer moves with the I overlayer. We never observed the separation of the TeO_2 dimers during these experiments, which supports their attractive interaction as predicted by DFT.

In summary, we find that ^{125}I monolayer films on Au(111) are remarkably stable when considering the ultrafast release of 185 keV of nuclear energy. This is due to the small nuclear recoil energy and strong hybridization with the metallic surface that prevents charging of the daughter Te atom during its electron emission cascades. DFT calculations reveal that the daughter Te atom is bound to the Au surface more strongly than the I, which itself forms a stable monolayer that is unreactive under ambient conditions. While Te is formed in its zero oxidation state, XPS reveals that exposure to ambient conditions causes oxidation to the 4+ oxidation state. Extensive DFT calculations indicate that reaction with molecular oxygen is exothermic and leads to the formation of TeO_2, consistent with the 4+ oxidation state measured by XPS. STM imaging and DFT-simulated images indicate that the surface-bound TeO_2 units pair up as Te_2O_4 dimers which, under the influence of the STM tip, freely diffuse with the I overlayer. DFT calculations show that dimer formation is exothermic, as evidenced by their predominance in the STM images. These data indicate that radioactive ^{125}I films are stable after exposure to ambient conditions and that the ^{125}Te daughter atoms are oxidized but remain surface-bound when exposed to ambient conditions.

CONCLUSIONS

The robust nature of the ^{125}I films during nuclear transmutation of I to Te bodes well for the application of radioactive films on both planar and Au nanoparticle substrates. The fact that the radioactive decay occurs *via* electron capture with low recoil energy renders these films robust with respect to autoradiolysis that plagues many α- and β-emitter constructs. Despite the importance of radioactive decay in a wide range of technologies, there is currently no other known air-stable 2D radiation sources. The reduced dimensionality of these surface-bound films provides the ability to study high-energy nuclear processes safely and enables the microscopic details of radiation chemistry, biological degradation, and material damage to be quantified. The enhanced electron emission results offer the intriguing prospect of using metal nanoparticle-supported radioisotopes for the enhanced, targeted electron dosing of tumor cells with short-range, chemically active low-energy electrons. We envisage a new field that combines nanoscience with radioisotopes, enabling understanding of many aspects of radiochemistry, physics, and biology, as well as offering new constructs for *in vivo* radioisotope delivery for cancer therapy. Furthermore, a microscopic picture of how radioactive atoms can be assembled on surfaces/nanoparticles, how they decay, and how the resulting radiation affects their local molecular environment will provide fundamental knowledge about both

materials and biological damage, uncover new non-equilibrium chemistries, fuel the discovery of methods for constructing nanoscale radioactive materials, and enable new technologies.

MATERIALS AND METHODS

Experimental. ^{125}I/Au(111) samples were made using the established ambient drop-casting method at PerkinElmer (Billerica, MA); drop-casting procedure and the resulting monolayer are shown in Figure 1.[1] A solution of Na^{125}I (161 μM) and NaOH in H$_2$O (pH 9) is dropped onto a clean Au(111) surface and dried under a constant stream of N$_2$ gas. The ^{125}I spontaneously chemisorbs to the Au(111) surface, saturating when a well-ordered single layer of ^{125}I is formed. After the droplet containing ^{125}I has dried, the sample is rinsed with methanol to remove any physisorbed material. While the deposition solution has a radionuclide purity of >99.9%, it typically has an age at the time of deposition that can result in up to 30% of the ^{125}I having already decayed into ^{125}Te, and hence, a lower chemical purity. However, despite the high concentration of Te in the deposition solution, we find that the amount of Te on our ^{125}I/Au samples when they first arrive at Tufts University (a few days after deposition) is no more than one would expect from the decay of a perfect ^{125}I monolayer. This is because the newly formed Te atoms in the deposition solution are formed in a highly charged state that makes them react with water in the surrounding solution to form telluric acid/hydrated oxide, which does not bind to Au. We imaged the ^{125}I/Au(111) film structure with an OmicronNanotechnology low-temperature STM operating at 5 K. XPS data as a function of time were taken at Tufts using a five-channel hemispherical energy analyzer. A ^{125}I/Au(111) sample was also sent to Carnegie Mellon University and used to measure high-resolution electron emission spectra using a hemispherical energy analyzer in a ThermoFisher ThetaProbe instrument. Given the importance of knowing the exact kinetic energy of the emitted electrons, and hence the oxidation state of the decaying atom, a total of 1500 individual scans were performed across the kinetic energy range from 430 to 530 eV with 190 eV pass energy (constant analyzer energy). Each scan was taken using 0.2 eV steps with a 100 ms dwell time per step. The kinetic energy calibration of the detector was verified by measuring the kinetic energy of electrons produced from a clean Ag standard by excitation with monochromated Al Kα X-rays. The Ag 3p$_{3/2}$ and Ag 3d$_{5/2}$ peaks were found to lie within $\pm$0.1 eV of the expected positions for metallic Ag of 913.7 and 1118.4 eV, respectively (corresponding to binding energies of 572.9 and 368.2 eV, respectively).

Theoretical. Density functional theory calculations were performed with the Perdew–Burke–Ernzerhof[39,40] exchange-correlation functional. The periodic plane wave DFT code VASP[41,42] was used to carry out all spin-polarized first-principles calculations. Core electrons were replaced by projector-augmented wave potentials,[43] and valence electrons were expanded in plane waves with a cutoff energy of 400 eV. A 4 atomic layer thick slab was used to model an unreconstructed Au(111) surface. The bottom two layers were kept fixed at their bulk truncated values, and every other atom was allowed to relax. Slabs were separated along the surface normal by a 15 Å thick vacuum region, and a dipole correction along the surface normal was applied for all calculations. Total energies were converged to a 1.0×10^{-6} eV accuracy, and ions were relaxed until the forces acting on them were below 0.005 eV/Å. For all formation energy calculations, a $2\sqrt{3} \times 2\sqrt{3}$ unit cell was used, and to explore the tendency of TeO$_2$ molecules to dimerize, a $4\sqrt{3} \times 4\sqrt{3}$ cell was used. In each case, a Monkhorst–Pack k-point mesh[44] equivalent to at least a $6 \times 6 \times 1$ mesh per $\sqrt{3} \times \sqrt{3}$ unit cell was used. STM images were calculated with a higher level of k-point convergence, specifically a $24 \times 24 \times 1$ Monkhorst–Pack k-point mesh per $\sqrt{3} \times \sqrt{3}$ unit cell at a -0.1 eV (i.e., looking at occupied states) bias using the Tersoff–Hamann approximation[45] with an s-like tip. Additional information on the calculations performed, including results with the optB88-vdW functional, is given in the Supporting Information.[50]

ASSOCIATED CONTENT

Ⓢ Supporting Information

The Supporting Information is available free of charge on the ACS Publications website at DOI: 10.1021/acsnano.5b06640.

Additional details about path-integral DFT and KMC simulations (PDF)

AUTHOR INFORMATION

Corresponding Authors
*E-mail: angelos.michaelides@ucl.ac.uk.
*E-mail: charles.sykes@tufts.edu.

Notes
The authors declare no competing financial interest.

REFERENCES

(1) Pronschinske, A.; Pedevilla, P.; Murphy, C. J.; Lewis, E. A.; Lucci, F. R.; Brown, G.; Pappas, G.; Michaelides, A.; Sykes, E. C. H. Enhancement of Low-Energy Electron Emission in 2D Radioactive Films. *Nat. Mater.* **2015**, *14*, 904−907.

(2) Arumainayagam, C. R.; Lee, H.-L.; Nelson, R. B.; Haines, D. R.; Gunawardane, R. P. Low-Energy Electron-Induced Reactions in Condensed Matter. *Surf. Sci. Rep.* **2010**, *65*, 1−44.

(3) Pimblott, S. M.; LaVerne, J. A. Production of Low-Energy Electrons by Ionizing Radiation. *Radiat. Phys. Chem.* **2007**, *76*, 1244−1247.

(4) Alizadeh, E.; Sanz, A. G.; Garcia, G.; Sanche, L. Radiation Damage to DNA: The Indirect Effect of Low-Energy Electrons. *J. Phys. Chem. Lett.* **2013**, *4*, 820−825.

(5) Simons, J. How Do Low-Energy (0.1−2 eV) Electrons Cause DNA Strand Breaks? *Acc. Chem. Res.* **2007**, *963*, 256−259.

(6) Barrios, R.; Skurski, P.; Simons, J. Mechanism for Damage to DNA by Low-Energy Electrons. *J. Phys. Chem. B* **2002**, *106*, 7991−7994.

(7) Boudaïffa, B.; Cloutier, P.; Hunting, D.; Huels, M. A.; Sanche, L. Resonant Formation of DNA Strand Breaks by Low-Energy (3 to 20 eV) Electrons. *Science* **2000**, *287*, 1658−1660.

(8) Alexander, W. A.; Wiens, J. P.; Minton, T. K.; Nathanson, G. M. Reactions of Solvated Electrons Initiated by Sodium Atom Ionization at the Vacuum-Liquid Interface. *Science* **2012**, *335*, 1072−1075.

(9) Alizadeh, E.; Sanche, L. Precursors of Solvated Electrons in Radiobiological Physics and Chemistry. *Chem. Rev.* **2012**, *112*, 5578−5602.

(10) Siefermann, K. R.; Liu, Y.; Lugovoy, E.; Link, O.; Faubel, M.; Buck, U.; Winter, B.; Abel, B. Binding Energies, Lifetimes and

Implications of Bulk and Interface Solvated Electrons in Water. *Nat. Chem.* **2010**, *2*, 274−279.

(11) Garrett, B. C.; Dixon, D. A.; Camaioni, D. M.; Chipman, D. M.; Johnson, M. A.; Jonah, C. D.; Kimmel, G. A.; Miller, J. H.; Rescigno, T. N.; Rossky, P. J.; Xantheas, S. S.; Colson, S. D.; Laufer, A. H.; Ray, D.; Barbara, P. F.; Bartels, D. M.; Becker, K. H.; Bowen, K. H.; Bradforth, S. E.; Carmichael, I.; et al. Role of Water in Electron-Initiated Processes and Radical Chemistry: Issues and Scientific Advances. *Chem. Rev.* **2005**, *105*, 355−389.

(12) Balagurumoorthy, P.; Xu, X. Effect of Distance between Decaying 125I and DNA on Auger-Electron Induced Double-Strand Break Yield. *Int. J. Radiat. Biol.* **2012**, *88*, 998−1008.

(13) Hervé Du Penhoat, M. A.; Huels, M. A.; Cloutier, P.; Jay-Gerin, J. P.; Sanche, L. Electron Stimulated Desorption of H- from Thin Films of Thymine and Uracil. *J. Chem. Phys.* **2001**, *114*, 5755−5764.

(14) Hainfeld, J. F.; Slatkin, D. N.; Smilowitz, H. M. The Use of Gold Nanoparticles to Enhance Radiotherapy in Mice. *Phys. Med. Biol.* **2004**, *49*, N309−N315.

(15) Zheng, Y.; Hunting, D. J.; Ayotte, P.; Sanche, L. Radio-sensitization of DNA by Gold Nanoparticles Irradiated with High-Energy Electrons. *Radiat. Res.* **2008**, *169*, 19−27.

(16) Martin, F.; Burrow, P. D.; Cai, Z.; Cloutier, P.; Hunting, D.; Sanche, L. DNA Strand Breaks Induced by 0−4 eV Electrons: The Role of Shape Resonances. *Phys. Rev. Lett.* **2004**, *93*, 6−9.

(17) Kim, Y. H.; Jeon, J.; Hong, S. H.; Rhim, W. K.; Lee, Y. S.; Youn, H.; Chung, J. K.; Lee, M. C.; Lee, D. S.; Kang, K. W.; Nam, J.-M. Tumor Targeting and Imaging Using Cyclic RGD-PEGylated Gold Nanoparticle Probes with Directly Conjugated Iodine-125. *Small* **2011**, *7*, 2052−2060.

(18) Dam, D. H. M.; Lee, J. H.; Sisco, P. N.; Co, D. T.; Zhang, M.; Wasielewski, M. R.; Odom, T. W. Direct Observation of Nanoparticle-Cancer Cell Nucleus Interactions. *ACS Nano* **2012**, *6*, 3318−3326.

(19) Gu, Y. J.; Cheng, J.; Lin, C. C.; Lam, Y. W.; Cheng, S. H.; Wong, W. T. Nuclear Penetration of Surface Functionalized Gold Nanoparticles. *Toxicol. Appl. Pharmacol.* **2009**, *237*, 196−204.

(20) Bardhan, R.; Lal, S.; Joshi, A.; Halas, N. J. Theranostic Nanoshells: From Probe Design to Imaging and Treatment of Cancer. *Acc. Chem. Res.* **2011**, *44*, 936−946.

(21) Ghosh, P.; Han, G.; De, M.; Kim, C. K.; Rotello, V. M. Gold Nanoparticles in Delivery Applications. *Adv. Drug Delivery Rev.* **2008**, *60*, 1307−1315.

(22) Craig, G. E.; Brown, S. D.; Lamprou, D. A.; Graham, D.; Wheate, N. J. Cisplatin-Tethered Gold Nanoparticles That Exhibit Enhanced Reproducibility, Drug Loading, and Stability: A Step Closer to Pharmaceutical Approval? *Inorg. Chem.* **2012**, *51*, 3490−3497.

(23) Cheng, W.; Dong, S.; Wang, E. Iodine-Induced Gold-Nanoparticle Fusion/fragmentation/aggregation and Iodine-Linked Nanostructured Assemblies on a Glass Substrate. *Angew. Chem., Int. Ed.* **2003**, *42*, 449−452.

(24) Huang, L.; Huang, L.; Zeppenfeld, P.; Zeppenfeld, P.; Horch, S.; Horch, S.; Comsa, G.; Comsa, G. Determination of Iodine Adlayer Structures on Au(111) by Scanning Tunneling Microscopy. *J. Chem. Phys.* **1997**, *107*, 585.

(25) Yamada, T.; Batina, N.; Itaya, K. Structure of Electrochemically Deposited Iodine Adlayer on Au(111) Studied by Ultrahigh-Vacuum Instrumentation and *in Situ* STM. *J. Phys. Chem.* **1995**, *99*, 8817−8823.

(26) Zhu, L. Neutrino-Recoil Induced Desorption. *J. Vac. Sci. Technol., A* **1994**, *12*, 2037.

(27) McLaughlin, M. F.; Woodward, J.; Boll, R. A.; Wall, J. S.; Rondinone, A. J.; Kennel, S. J.; Mirzadeh, S.; Robertson, J. D. Gold Coated Lanthanide Phosphate Nanoparticles for Targeted Alpha Generator Radiotherapy. *PLoS One* **2013**, *8*, 2−9.

(28) Hsiung, C.; Gordus, A. A. Momentum Transfer to an Atom in a Molecule: Internal Excitation and Bond Dissociation. *J. Chem. Phys.* **1962**, *36*, 947.

(29) Booth, C. H.; Bauer, E. D.; Daniel, M.; Wilson, R. E.; Mitchell, J. N.; Morales, L. A.; Sarrao, J. L.; Allen, P. G. Quantifying Structural Damage from Self-Irradiation in a Plutonium Superconductor. *Phys. Rev. B - Condens. Matter Mater. Phys.* **2007**, *76*, 1−7.

(30) Farnan, I.; Cho, H.; Weber, W. J. Quantification of Actinide Alpha-Radiation Damage in Minerals and Ceramics. *Nature* **2007**, *445*, 190−193.

(31) Suggs, D. W.; Stickney, J. L. Characterization of Atomic Layers of Tellurium Electrodeposited on the Low-Index Planes on Gold. *J. Phys. Chem.* **1991**, *95*, 10056−10064.

(32) Sorenson, T. A. A Comparison of Atomic Layers Formed by Electrodeposition of Selenium and Tellurium Scanning Tunneling Microscopy Studies on Au(100) and Au(111). *J. Electrochem. Soc.* **1999**, *146*, 1019.

(33) Verkhoturov, S. V.; Schweikert, E. a; Chechik, V.; Sabapathy, R. C.; Crooks, R. M.; Parilis, E. S. Auger Stimulated Ion Desorption of Negative Ions *via* K-Capture Radioactive Decay. *Phys. Rev. Lett.* **2001**, *87*, 037601.

(34) Gokhberg, K.; Kolorenč, P.; Kuleff, A. I.; Cederbaum, L. S. Site- and Energy-Selective Slow-Electron Production through Intermolecular Coulombic Decay. *Nature* **2014**, *505*, 661−663.

(35) Nath, A.; Prushan, M. J.; Gilbert, J. G. Can Super-Excited Molecules Survive Fragmentation? *J. Radioanal. Nucl. Chem.* **2001**, *247*, 589−591.

(36) Carlson, T. A.; White, R. M. Formation of Fragment Ions from CH3Te125 and C2H5Te125 Following the Nuclear Decays of CH3I125 and C2H5I125. *J. Chem. Phys.* **1963**, *38*, 2930.

(37) Pomplun, A. E.; Booz, J.; Charlton, D. E.; Pomplun, E. A Monte Carlo Simulation of Auger Cascades. *Radiat. Res.* **1987**, *111*, 533−552.

(38) Kolasinski, K. *Surface Science: Foundations of Catalysis and Nanoscience*; Wiley, 2012.

(39) Perdew, J. P.; Burke, K.; Ernzerhof, M. Generalized Gradient Approximation Made Simple. *Phys. Rev. Lett.* **1996**, *77*, 3865.

(40) Perdew, J. P.; Burke, K.; Ernzerhof, M. Generalized Gradient Approximation Made Simple- ERRATA. *Phys. Rev. Lett.* **1996**, *77*, 3865−3868.

(41) Kresse, G.; Hafner, J. *Ab Initio* Molecular Dynamics of Liquid Metals. *Phys. Rev. B: Condens. Matter Mater. Phys.* **1993**, *47*, 558−561.

(42) Kresse, G.; Furthmüller, J. Efficient Iterative Schemes for *Ab Initio* Total-Energy Calculations Using a Plane-Wave Basis Set. *Phys. Rev. B: Condens. Matter Mater. Phys.* **1996**, *54*, 11169−11186.

(43) Kresse, G.; Joubert, D. From Ultrasoft Pseudopotentials to the Projector Augmented-Wave Method. *Phys. Rev. B: Condens. Matter Mater. Phys.* **1999**, *59*, 1758−1775.

(44) Monkhorst, H. J.; Pack, J. D. Special Points for Brillouin-Zone Integrations. *Phys. Rev. B* **1976**, *13*, 5188−5192.

(45) Tersoff, J.; Hamann, D. R. Theory of the Scanning Tunneling Microscope. *Phys. Rev. B: Condens. Matter Mater. Phys.* **1985**, *31*, 805−813.

(46) Charlton, D. E.; Booz, J. A Monte Carlo Treatment of the Decay of 125I. *Radiat. Res.* **1981**, *87*, 10−23.

(47) Bahl, M. K.; Watson, R. L.; Irgolic, K. J. X-Ray Photoemission Studies of Tellurium and Some of Its Compounds. *J. Chem. Phys.* **1977**, *66*, 5526.

(48) Detty, M.; Lenhart, W. C.; Gassman, P. G.; Callstrom, M. R. XPS and 125Te NMR Studies of Organotellurium Compounds. 1. Tellurapyrans, Tellurapyranones, Tellurapyrylium Salts, and Their Benzo Analogues in Both the Tellurium(II) and Tellurium(IV) Oxidation States. *Organometallics* **1989**, *8*, 861−865.

(49) Chastain, J.; Moulder, J. F. *Handbook of X-ray Photoelectron Spectroscopy: A Reference Book of Standard Spectra for Identification and Interpretation of XPS Data*; Physical Electronics, 1995.

(50) Klimeš, J.; Bowler, D. R.; Michaelides, A. Van Der Waals Density Functionals Applied to Solids. *Phys. Rev. B: Condens. Matter Mater. Phys.* **2011**, *83*, 195131.